J. Mech. Phys. Solids Vol. 40, No. 2, pp. 339–372, 1992.
Printed in Great Britain.

0022–5096/92 $5.00 + 0.00
© 1992 Pergamon Press plc

MEASUREMENT OF TRANSIENT CRACK-TIP DEFORMATION FIELDS USING THE METHOD OF COHERENT GRADIENT SENSING

SRIDHAR KRISHNASWAMY,† HAREESH V. TIPPUR‡ and ARES J. ROSAKIS§

Graduate Aeronautical Laboratories, California Institute of Technology,
Pasadena, CA 91125, U.S.A.

(*Received* 26 *July* 1990; *in revised form* 28 *January* 1991)

ABSTRACT

A SHEARING interferometric method (CGS) is proposed as a viable alternative to currently used experimental techniques for the study of dynamic crack propagation in both transparent and opaque media. CGS is a full-field optical technique that provides real-time fringes representing crack-tip deformation or stress state. The results of the experiments are interpreted on the basis of the conventional singular asymptotic analysis as well as a newly developed transient higher-order asymptotic analysis. The excellent agreement obtained between the experimental results and the *higher-order* asymptotic analysis clearly indicates that the contribution of the non-singular terms to the total stress and deformation fields is too important to be ignored.

1. INTRODUCTION

OPTICAL techniques have been used extensively in the direct determination of transient crack-tip fields in an effort to investigate rapid crack propagation failure criteria. The method of photoelasticity, for instance, has been used to obtain dynamic fracture toughness of a variety of transparent, optically anisotropic materials such as Homalite-100 (KOBAYASHI and DALLY, 1977). The method of caustics has been used to study the fracture behavior of both transparent materials such as PMMA and Homalite-100 (RAVI-CHANDAR and KNAUSS, 1984; KALTHOFF, 1985) and opaque materials such as steel (ROSAKIS *et al.*, 1984; KALTHOFF, 1985; ZEHNDER and ROSAKIS, 1989). Unlike photoelasticity, however, the method of caustics is not a full-field technique. There has thus been a need for a *full-field* technique that would work well with materials which are either opaque or which are not optically birefringent.

In this paper, we present a shearing interferometric technique—*coherent gradient sensing* (*CGS*)—which can be used to obtain *full-field* information of dynamic crack-tip deformation in both opaque and optically isotropic transparent solids. Unlike the shearing interferometer used by BALAS and DRZIK (1983) in their study of *static*

† Present address: Department of Mechanical Engineering, Northwestern University, Chicago, IL 60208, U.S.A.

‡ Present address: Department of Mechanical Engineering, Auburn University, Auburn, AL 36849, U.S.A.

§ Author to whom correspondence should be addressed.

mixed-mode crack-tip fields, the set-up discussed in this paper is particularly suited for real-time study of rapidly propagating cracks. While all necessary details of the CGS technique will be presented here, a more complete description of the method, an account of related optical techniques, and results of a companion study pertaining to static crack-tip deformation fields may be found in TIPPUR *et al.* (1989a, b). The purpose of the present investigation is two-fold. We show the feasibility of applying the method of CGS in both transmission and reflection modes to map transient crack-tip deformation fields in materials such as PMMA and AISI 4340 steel. We then devote attention toward clarifying certain issues regarding the interpretation of the experimental results on the basis of both existing asymptotic analyses and more complete transient higher-order descriptions.

2. THE METHOD OF COHERENT GRADIENT SENSING

In Fig. 1 the schematic of the experimental set-up used for transmission CGS is shown. A transparent, optically isotropic specimen is illuminated by a collimated beam of coherent laser light. The transmitted object wave is then incident on a pair of high-density Ronchi gratings, G_1 and G_2, separated by a distance Δ. The diffracted wavefronts emerging from grating G_2 are collected through a filtering lens L_1. The frequency content (diffraction spectrum) of the field distribution on the G_2-plane is thus obtained on the back focal plane of the filtering lens. A filtering aperture is

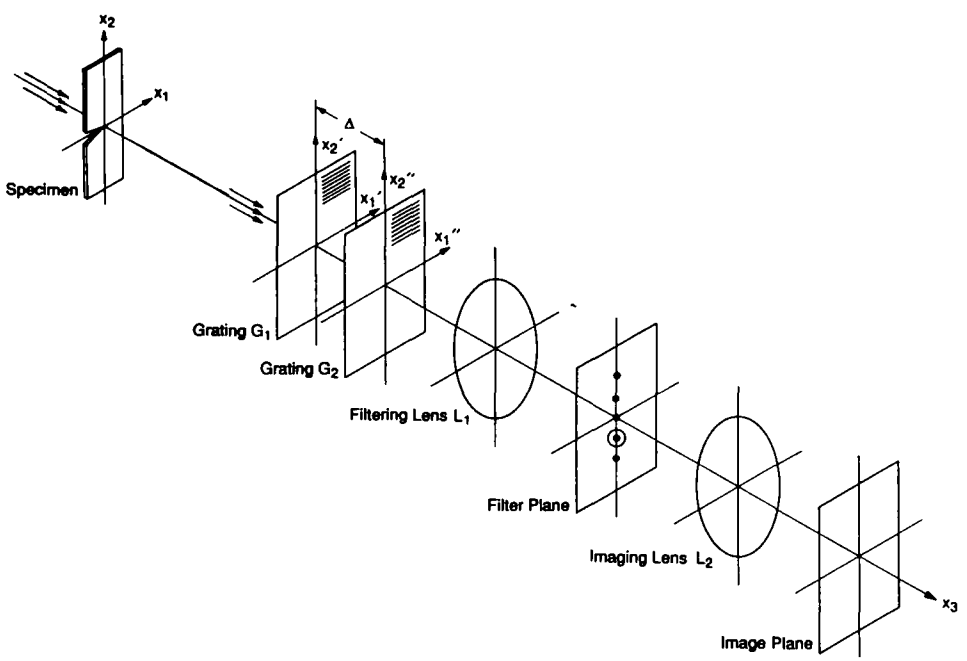

FIG. 1. Transmission CGS set-up schematic.

located on the back focal plane of lens L_1 so as to block all but the ± 1 diffraction order. The filtered beam is then further imaged by means of a system of lenses (denoted here by a single lens L_2 for simplicity) on to the image plane of a high-speed camera.

Figure 2 shows the modification of the above set-up for measuring surface slopes of opaque solids when CGS is used in reflection mode. In this case, the specularly reflecting object surface is illuminated normally by a collimated beam of laser light using a beam splitter. The reflected beam, as in transmission mode, then gets processed through the optical arrangement which is identical to the one shown in Fig. 1.

In the following sections, a first-order diffraction analysis is presented which demonstrates that the information obtained on the image plane corresponds to in-plane stress gradients in transmission mode, and out-of-plane displacement gradients in reflection mode.

2.1. *Principle*

Figure 3 explains the working principle of the method of CGS. For the sake of simplicity, and without losing generality, the line gratings are assumed to have a sinusoidal transmittance. Let the gratings G_1 and G_2 have their rulings parallel to, say, the x_1-axis. A plane wave transmitted through or reflected from an undeformed specimen and propagating along the optical axis is diffracted into three plane wave fronts E_0, E_1 and E_{-1} by the first grating G_1. The magnitude of the angle between the propagation directions of E_0 and $E_{\pm 1}$ is given by the diffraction equation $\theta = \sin^{-1}(\lambda/p)$, where λ is the wavelength and p is the grating pitch. Upon incidence

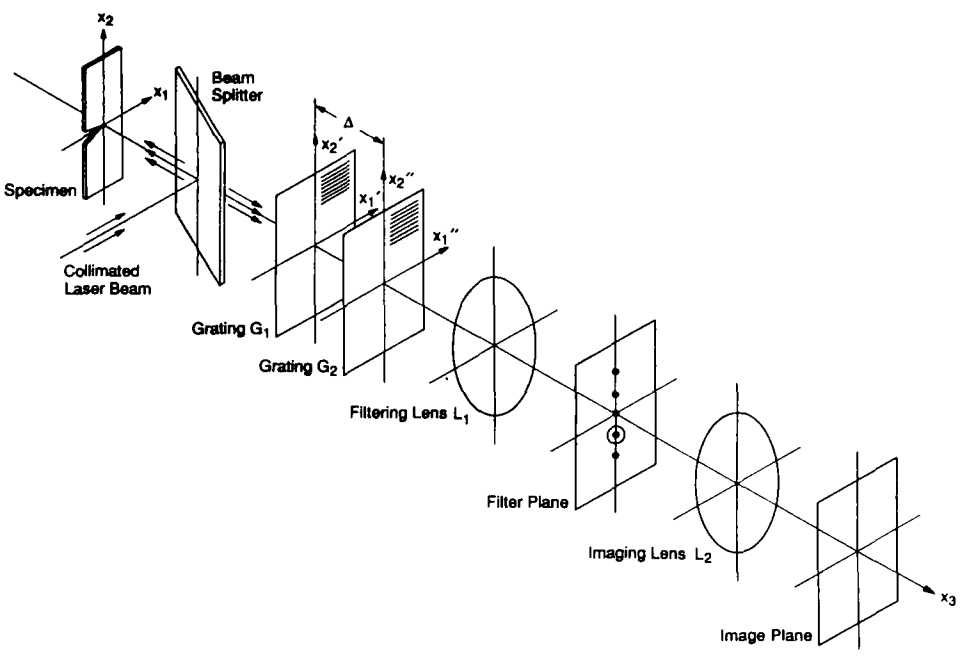

FIG. 2. Reflection CGS set-up schematic.

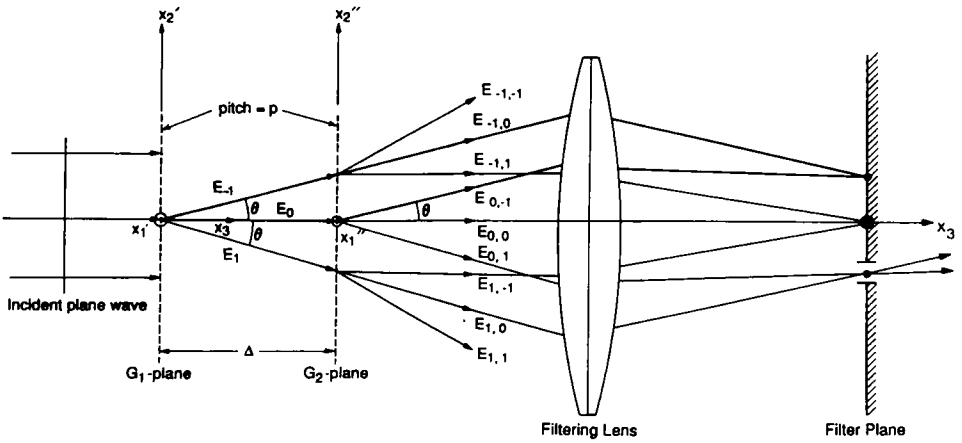

FIG. 3. Working principle.

on the second grating G_2, the wave fronts are further diffracted into $E_{0,0}$, $E_{0,1}$, $E_{1,-1}$, $E_{1,0}$, $E_{1,1}$ etc. These wave fronts which are propagating in distinctly different directions are then brought to focus at spatially separated diffraction spots on the back focal plane of the filtering lens. The spacing between these diffraction spots is directly proportional to sin θ or inversely proportional to the grating pitch.

Now, consider a plane wave normally incident on a *deformed* specimen surface. The resulting transmitted or reflected wave front will be distorted either due to changes in the refractive index of the material or due to non-uniform surface deformations. This object wave front that is incident on G_1 now carries information regarding the specimen deformation, and consists of light rays travelling with perturbations to their initial direction parallel to the optical axis. Thus, each of the diffraction spots on the focal plane of L_1 will now be locally surrounded by a halo of dispersed light field due to the deflected rays. The extent of this depends on the nature of the deformations. By using a two-dimensional aperture at the filtering plane, information existing around one of the spots can be further imaged. Here, an important but subtle point should be noted. Since each of the diffraction spots is surrounded by dispersed light due to the deformation, overlapping of the information from different diffracted orders could occur on the filtering plane when the deflection of the ray is sufficiently large [i.e. $\geqslant(\lambda/2p)$]. However, as will be shown in the following sections, this limitation can easily be overcome by the use of higher density gratings.

2.2. *Analysis*

Consider a specimen whose midplane, in transmission mode, or surface, in reflection mode, occupies the (x_1, x_2) plane in the undeformed state (Fig. 4). Let $\mathbf{e}_i$ denote unit vectors along the x_i-axis ($i = 1, 2, 3$). When the specimen is undeformed, the object wave propagation vector is along $\mathbf{d}_0 = \mathbf{e}_3$. After deformation, the propagation vector is perturbed and can be expressed by

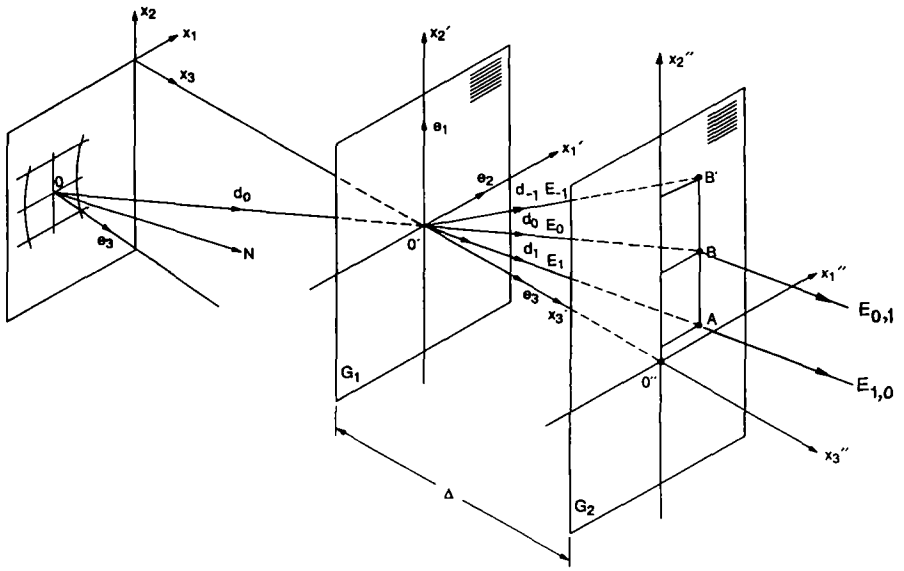

FIG. 4. Diffraction of a generic bundle.

$$\mathbf{d}_0 = \alpha \mathbf{e}_1 + \beta \mathbf{e}_2 + \gamma \mathbf{e}_3, \tag{1}$$

where $\alpha(x_1, x_2)$, $\beta(x_1, x_2)$, and $\gamma(x_1, x_2)$ denote the direction cosines of the propagation vector of the perturbed wave front. The object wave front, upon incidence on the sinusoidal grating G_1, whose principal direction (defined as the direction perpendicular to the grating lines) is parallel to, say, the x_2-axis, is diffracted into three wave fronts propagating along $\mathbf{d}_0$ and $\mathbf{d}_{\pm 1}$ and whose amplitudes $E_0(\mathbf{x}')$ and $E_{\pm 1}(\mathbf{x}')$ can be represented by

$$E_0(\mathbf{x}') = a_0 \exp(ik\mathbf{d}_0 \cdot \mathbf{x}'), \quad E_{\pm 1}(\mathbf{x}') = a_{\pm 1} \exp(ik\mathbf{d}_{\pm 1} \cdot \mathbf{x}'), \tag{2}$$

where a_0 and $a_{\pm 1}$ are constants and $k = 2\pi/\lambda$ is the wave number. The propagation directions of the first-order diffracted wave fronts can be related to the direction cosines of the incident propagation vector through

$$\mathbf{d}_{\pm 1} = [\alpha \mathbf{e}_1 + (\beta \cos\theta \pm \gamma \sin\theta)\mathbf{e}_2 + (\gamma \cos\theta \mp \beta \sin\theta)\mathbf{e}_3], \tag{3}$$

using the diffraction condition $\theta = \sin^{-1}(\lambda/p)$ [see TIPPUR *et al.* (1989a) for details]. Evaluating the amplitude distribution of three diffracted wave fronts on plane G_2 ($x_3' = \Delta$) (see Fig. 4), we find that

$$E_0|_{x_3'=\Delta} = a_0 \exp\left(\frac{ik\Delta}{\gamma}\right), \tag{4}$$

$$E_{\pm 1}|_{x_3'=\Delta} = a_{\pm 1} \exp\left(\frac{ik\Delta}{\gamma \cos\theta \mp \beta \sin\theta}\right). \tag{5}$$

The wave fronts E_0 and $E_{\pm 1}$ will each undergo further diffraction upon incidence on G_2, leading to secondary wave fronts $E_{0,0}$, $E_{0,1}$, $E_{1,-1}$, $E_{1,0}$, $E_{1,1}$ etc. Of these secondary diffractions, $E_{0,1}$ and $E_{1,0}$ have their propagation direction along $\mathbf{d}_1$, $E_{0,-1}$ and $E_{-1,0}$ along $\mathbf{d}_{-1}$, and $E_{0,0}$, $E_{-1,1}$ and $E_{1,-1}$ along $\mathbf{d}_0$ (Fig. 3). If information is spatially filtered by blocking all but the ± 1 diffraction order, only the wave fronts $E_{0,\pm 1}$ and $E_{\pm 1,0}$ contribute to the formation of the image. Note that the relative phase differences acquired by these two wave fronts is only in their travel from plane G_1 to plane G_2. Thus the amplitude distribution on the image plane is

$$E_{\text{im}} = (E_0 + E_{\pm 1})|_{x_3'=\Delta} = a_0 \exp\left(\frac{ik\Delta}{\gamma}\right) + a_{\pm 1} \exp\left(\frac{ik\Delta}{\gamma \cos\theta \mp \beta \sin\theta}\right). \tag{6}$$

Hence, the intensity distribution on the image plane is

$$I_{\text{im}} = E_{\text{im}} E_{\text{im}}^* \approx a_0^2 + a_{\pm 1}^2 + 2a_0 a_{\pm 1} \cos(k\Delta\beta\theta), \tag{7}$$

where E_{im}^* is the complex conjugate of E_{im}; and small θ and paraxial approximations (leading to $\gamma \approx 1$) are made. Thus, I_{im} denotes an intensity variation on the image plane whose maxima occur when

$$k\Delta\beta\theta = 2n\pi, \quad n = 0, \pm 1, \pm 2, \ldots, \tag{8}$$

when n denotes fringe order. In like manner, when the principal direction of the grating is parallel to the x_1-axis, it can be shown that fringe maxima correspond to

$$k\Delta\alpha\theta = 2m\pi, \quad m = 0, \pm 1, \pm 2, \ldots \tag{9}$$

Equations (8) and (9) are the fringe relations governing the method of CGS and they relate fringe orders to the direction cosines of the object wave front. It is clear from (8) and (9) that the sensitivity of the method could be increased by either increasing the grating separation distance Δ or decreasing the grating pitch p. Also note that there is a spatial uncertainty of $\delta = \Delta \tan\theta$ in the direction of shearing. This is due to our tacit approximation that the propagation vector of the deformed wave front is constant over the shearing length δ. This uncertainty in spatial location is typical of all shearing interferometers, and is unavoidable.

2.3. *Relation between direction cosines and deformation*

We now relate the direction cosines of the object wave front to deformation quantities of interest for both transmission and reflection cases.

2.3.1. *Transmission.* Consider a planar wave front incident normal to an optically isotropic, transparent plate of uniform nominal thickness h and refractive index n_0. Now, if the plate is deformed, the transmitted wave front acquires an optical path change δS which is given by the elasto-optical equation (ROSAKIS and RAVI-CHANDAR, 1986)

$$\delta S(x_1, x_2) = 2h(n_0 - 1)\int_0^{1/2} \varepsilon_{33}\, \mathrm{d}(x_3/h) + 2h\int_0^{1/2} \delta n_0\, \mathrm{d}(x_3/h). \tag{10}$$

The first term represents the net optical path difference due to the plate thickness change caused by the strain component ε_{33}. The second term is due to the stress-induced change in the refractive index of the material. This change in the refractive index δn_0 is given by the Maxwell relation (BEINERT and KALTHOFF, 1981)

$$\delta n_0(x_1, x_2) = D_1(\sigma_{11} + \sigma_{22} + \sigma_{33}), \tag{11}$$

where D_1 is a stress-optic constant and σ_{ij} are stress components. For an isotropic, linear elastic solid, the strain component ε_{33} can be related to stresses and thus (10) can be written as

$$\delta S = 2ch\int_0^{1/2} \left((\sigma_{11} + \sigma_{22}) \left\{ 1 + D_2 \left[\frac{\sigma_{33}}{\nu(\sigma_{11} + \sigma_{22})} \right] \right\} \right) \mathrm{d}(x_3/h), \tag{12}$$

where $c = D_1 - \nu(n_0 - 1)/E$, D_2 is a modified stress optic constant [see TIPPUR *et al.* (1988a)], and E and ν are the Young's modulus and Poisson's ratio of the material, respectively. Equation (12) is written in such a way that the term in the square brackets represents the degree of plane strain. When plane stress is a good approximation, this term can be neglected and (12) reduces to

$$\delta S \approx ch(\hat{\sigma}_{11} + \hat{\sigma}_{22}), \tag{13}$$

where $\hat{\sigma}_{11}$ and $\hat{\sigma}_{22}$ are thickness averages of stress components. The deformed object wave front is then described by $S(x_1, x_2, x_3) = x_3 + \delta S(x_1, x_2) = \text{constant}$. The propagation vector for the object wave front is, by definition, a unit vector normal to the wave front and is given by

$$\mathbf{d}_0 = \frac{\nabla(S)}{|\nabla(S)|} \approx \frac{\partial(\delta S)}{\partial x_1}\mathbf{e}_1 + \frac{\partial(\delta S)}{\partial x_2}\mathbf{e}_2 + \mathbf{e}_3 \tag{14}$$

for $|\nabla(\delta S)|^2 \ll 1$. Thus, using (13) and (14) in the fringe relations (8) and (9), the fringes are seen to be related to the gradients of stress quantities through

$$ch\frac{\partial}{\partial x_1}(\hat{\sigma}_{11} + \hat{\sigma}_{22}) = \frac{mp}{\Delta}, \tag{15}$$

$$ch\frac{\partial}{\partial x_2}(\hat{\sigma}_{11} + \hat{\sigma}_{22}) = \frac{np}{\Delta}. \tag{16}$$

2.3.2. *Reflection.* Consider a specimen whose reflective surface occupies the (x_1, x_2) plane in the undeformed state. Upon deformation, the reflector can be expressed as

$$F(x_1, x_2, x_3) = x_3 + u_3(x_1, x_2) = 0, \tag{17}$$

where u_3 is the out-of-plane displacement component. The unit surface normal $\mathbf{N}$ at a generic point $O(x_1, x_2)$ is given by

$$\mathbf{N} = \frac{\nabla F}{|\nabla F|} = \frac{u_{3,1}\mathbf{e}_1 + u_{3,2}\mathbf{e}_2 + \mathbf{e}_3}{\sqrt{1 + u_{3,1}^2 + u_{3,2}^2}}, \tag{18}$$

where $u_{3,\alpha}$ implies differentiation of u_3 with respect to x_α. Consider now a plane wave which is incident on the specimen along the $-x_3$-direction. From the law of reflection, and noting that vectors $\mathbf{d}_0$, $\mathbf{N}$ and $\mathbf{e}_3$ are coplanar, the propagation vector $\mathbf{d}_0$ of the reflected wave front is seen to be related to the gradients of u_3 through

$$\mathbf{d}_0 \approx 2u_{3,1}\mathbf{e}_1 + 2u_{3,2}\mathbf{e}_2 + \mathbf{e}_3, \tag{19}$$

where it is assumed that $|\nabla u_3|^2 \ll 1$. Using the above in the fringe relations (8) and (9), we find that

$$\frac{\partial u_3}{\partial x_1} = \left(\frac{mp}{2\Delta}\right) \quad m = 0, \pm 1, \pm 2, \ldots, \tag{20}$$

$$\frac{\partial u_3}{\partial x_2} = \left(\frac{np}{2\Delta}\right) \quad n = 0, \pm 1, \pm 2, \ldots, \tag{21}$$

where the relations $\theta \approx (\lambda/p)$ and $k = 2\pi/\lambda$ are made use of. For an isotropic, linear elastic solid, the out-of-plane displacement u_3 can be expressed as follows:

$$u_3 = -\frac{\nu h}{E}\int_0^{1/2}\left((\sigma_{11}+\sigma_{22})\left\{1-\left[\frac{\sigma_{33}}{\nu(\sigma_{11}+\sigma_{22})}\right]\right\}\right)\mathrm{d}(x_3/h). \tag{22}$$

In the above, the term in the square brackets represents the degree of plane strain and, when plane stress is a good approximation, it can be neglected. Thus, (22) reduces to

$$u_3 \approx -\frac{\nu h}{2E}(\hat{\sigma}_{11}+\hat{\sigma}_{22}). \tag{23}$$

Hence, from (20) and (21):

$$\frac{\partial u_3}{\partial x_1} = -\frac{\nu h}{2E}\frac{\partial}{\partial x_1}(\hat{\sigma}_{11}+\hat{\sigma}_{22}) = \left(\frac{mp}{2\Delta}\right) \quad m = 0, \pm 1, \pm 2, \ldots, \tag{24}$$

$$\frac{\partial u_3}{\partial x_2} = -\frac{\nu h}{2E}\frac{\partial}{\partial x_2}(\hat{\sigma}_{11}+\hat{\sigma}_{22}) = \left(\frac{np}{2\Delta}\right) \quad n = 0, \pm 1, \pm 2, \ldots. \tag{25}$$

3. EXPERIMENTS

Experiments were performed on PMMA specimens in both transmission and reflection modes, and on AISI 4340 steel specimens in reflection mode.

3.1. *Specimen preparation*

The specimen geometry used is shown in Fig. 5. The nominal specimen dimensions were length $2l = 15.2$ cm, width $w = 12.7$ cm, and thickness $h = 1$ cm. For CGS in transmission mode, specimens were made from a flat sheet of PMMA. A band saw, approximately 0.75 mm thick, was used to cut an initial notch of length $a = 25$ mm in these specimens. In the reflection mode, both PMMA and AISI 4340 steel specimens were used. For PMMA, an aluminum coating was applied to the specimen surface through a vacuum deposition technique in order to make it reflective. For AISI 4340 steel specimens, an initial notch of length $a = 38$ mm and root radius 0.15 mm was made through electric discharge machining. The steel specimens were heat-treated so as to obtain a nominally brittle material with a yield stress in uniaxial tension of $\sigma_0 \approx 1700$ MPa. After the preliminary machining and heat-treatment processes were completed, one face and the edges of each specimen were ground to ensure flatness and perpendicularity. The ground surface was lapped and then polished using a diamond polishing compound through a sequence of nine, six, three and one micron step to obtain an optically-flat, reflective surface. An aluminum coating was then applied to the specimen surface to further increase its reflectivity.

3.2. *Loading device*

The specimens were loaded in a three-point bending configuration. The loading device used to dynamically load the specimens was the Dynatup 8100A drop-weight tower which works as follows. A drop-weight whose mass and impact velocity can be varied to provide a range of impact energies, slides on two rails and can be hoisted to the desired height to obtain impact velocities of up to 10 m s^{-1}. A pneumatic valve releases the weight from the chain in free-fall. The hammer mounted at the bottom of the falling drop-weight impacts the specimen which then gets dynamically loaded to the point of crack initiation, whence the crack propagates rapidly through the

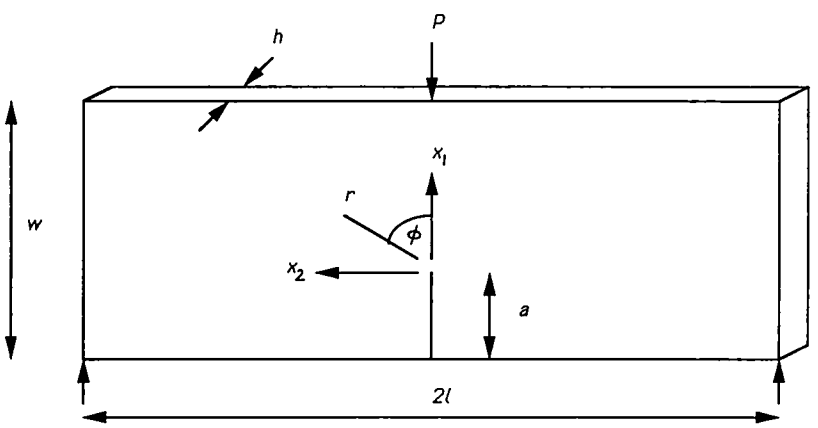

FIG. 5. Specimen geometry.

specimen. The experimental configuration is such that the crack is under mode-I loading conditions.

3.3. *High-speed photography*

A high-speed camera set-up (Fig. 6) was used to obtain a sequence of dynamic CGS interferograms. A Spectra Physics (model 166) argon-ion pulse laser (output power 2 W at $\lambda = 514$ nm in continuous-wave mode) was used as the light source. The laser beam was expanded and collimated to obtain a beam 50 mm in diameter which was centered on the initial notch tip of the specimen. The transmitted (in transmission mode) or reflected (in reflection mode) object wave front was then processed through a pair of line gratings of density 40 lines/mm with a separation distance $\Delta = 30$ mm. The gratings were oriented with their principal direction either parallel or perpendicular to the crack line in order to obtain either the x_1- or x_2-gradient information of the crack-tip fields. The resulting diffracted wavefronts were then collected, filtered and imaged onto a rotating-mirror high-speed camera through a series of lenses.

The camera consists of a 45° mirror mounted on the rotating shaft of a high-speed turbine. The in-coming light beam that enters the camera along the axis of the turbine is thus swept onto the film track by the mirror as it rotates. To obtain discrete pictures, the pulsing circuit of the laser was nominally set to give 50-ns exposure every 7–10 μs for a total of 1 ms from the time of an input trigger. Since the camera mirror was set to rotate at 800 rps, the above settings ensured that picture blur was minimal and also avoided overlap of frames while providing an adequate time-window for capturing the dynamic loading and crack-propagation event. The input trigger that initiates the pulsing of the laser was provided by a mechanical interrupt type photo-diode switch mounted on the fixed tower of the drop-weight machine. The switch was so positioned that the falling weight itself would activate it at the moment of impact of the hammer with the specimen.

4. RESULTS

The time sequence of CGS interferograms mapping the transient crack-tip deformation fields are analyzed in this section. In the first part, the analysis of fringe patterns is attempted under the assumption of K_I^d-dominance; that is, it is assumed that the stress and displacement fields all around the crack tip are well described by the asymptotic, square-root singular, dynamic stress-intensity factor (K_I^d) term. The inadequacies of this approach are then discussed, and a scheme for interpretation of CGS fringes using a more full-field description is discussed.

4.1. *Fringe interpretation under* K_I^d*-dominance assumption*

FREUND and CLIFTON (1974) have shown that the stress field with reference to a Cartesian coordinate system moving with a propagating crack tip for all *plane* elastodynamic solutions for smoothly running cracks under mode-I conditions can be asymptotically described by the square-root singular expression

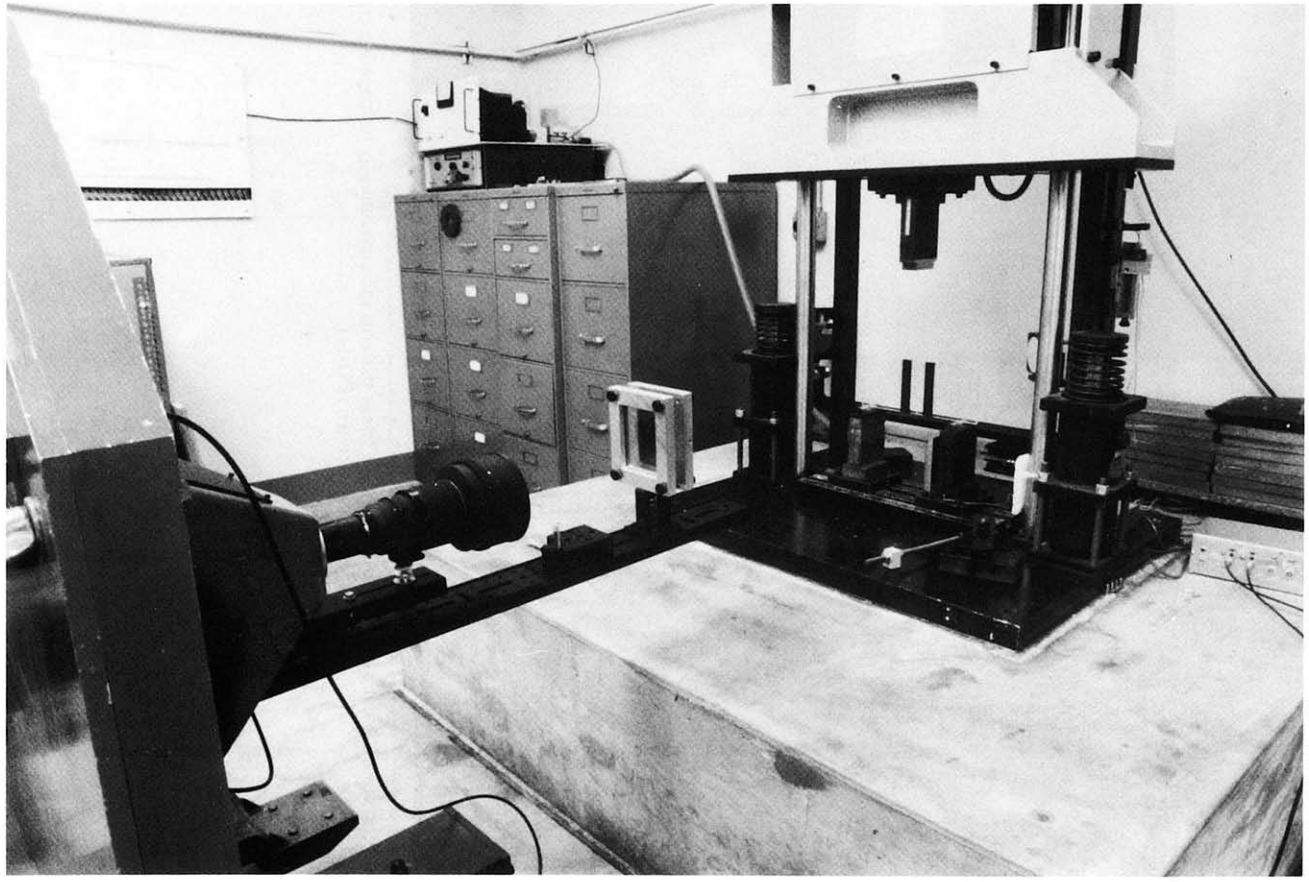

FIG. 6. Photograph of experimental set-up.

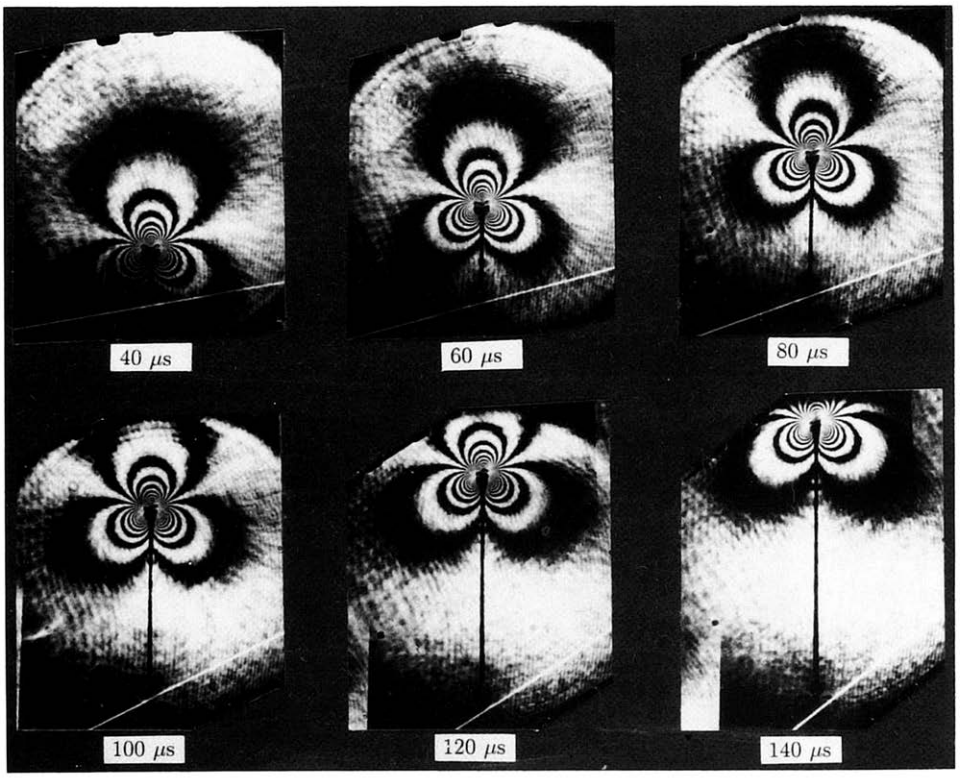

FIG. 7. (a) Sequence of transmission CGS x_1-gradient fringe patterns for a dynamically propagating crack in PMMA specimen (PD-11).

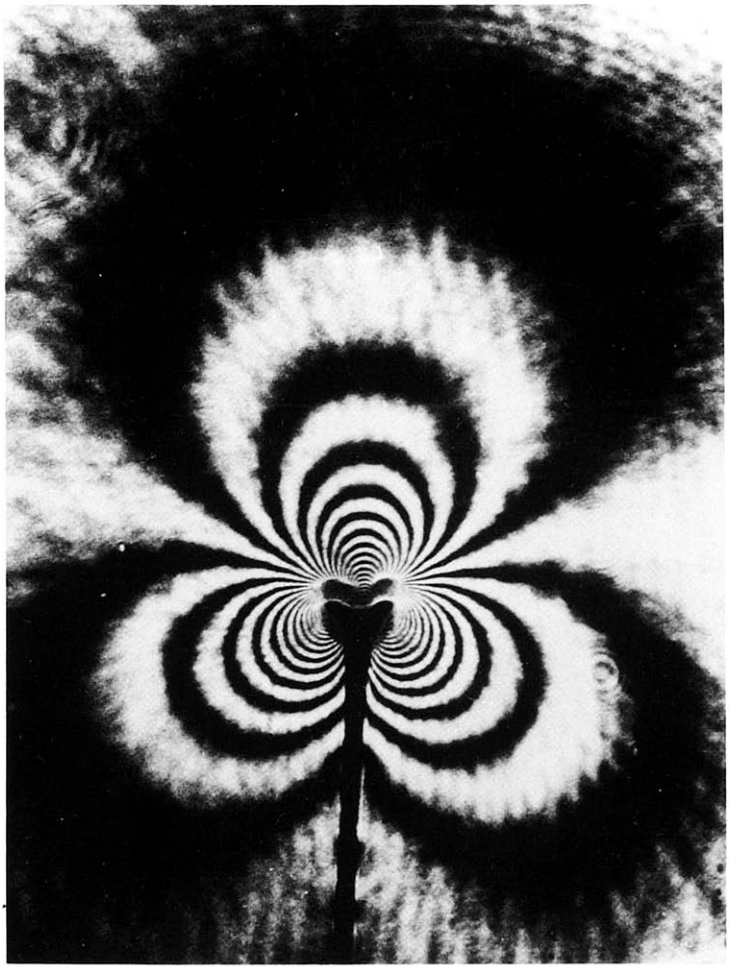

FIG. 7. (b) Enlarged view of transmission CGS x_1-gradient fringe pattern for a dynamically propagating crack in PMMA specimen (PD-11).

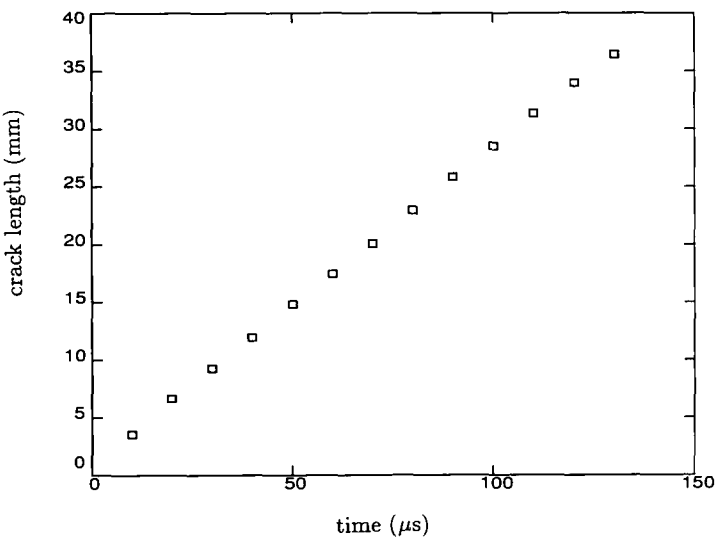

FIG. 7. (c). Crack-tip location as a function of time for a dynamically propagating crack in PMMA specimen (PD-11).

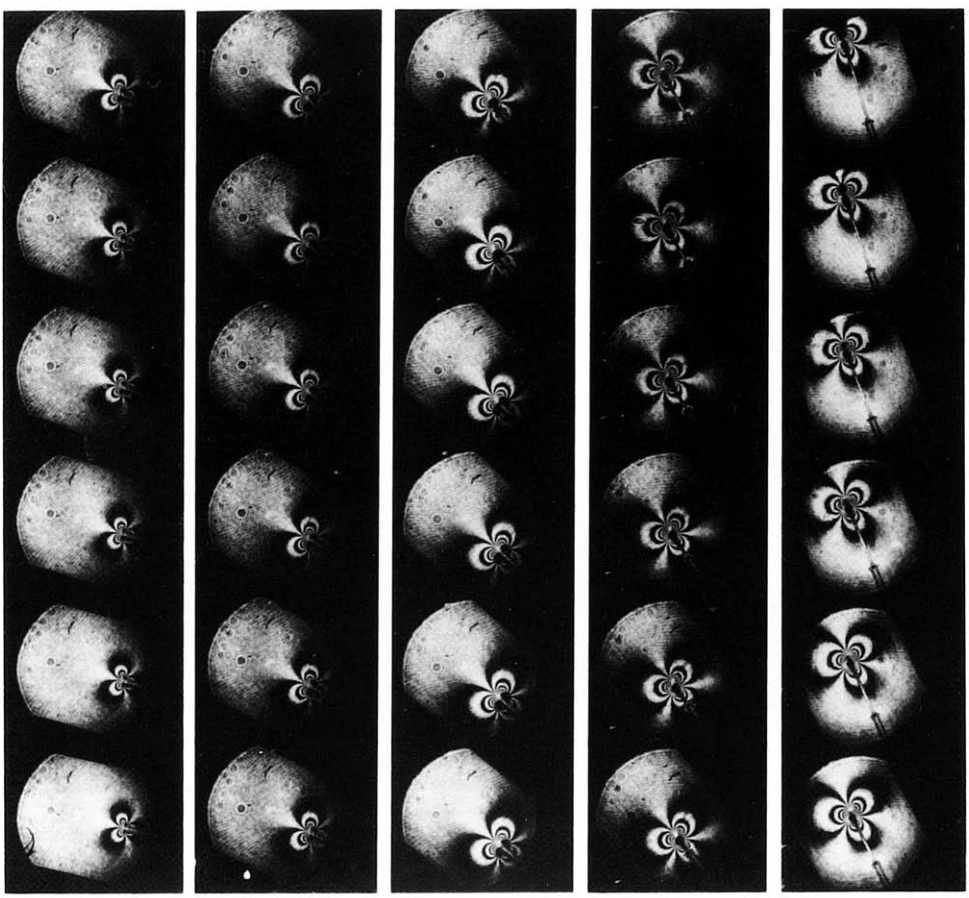

FIG. 8. Sequence of transmission CGS x_2-gradient fringe patterns for a dynamically propagating crack in PMMA specimen (PD-18).

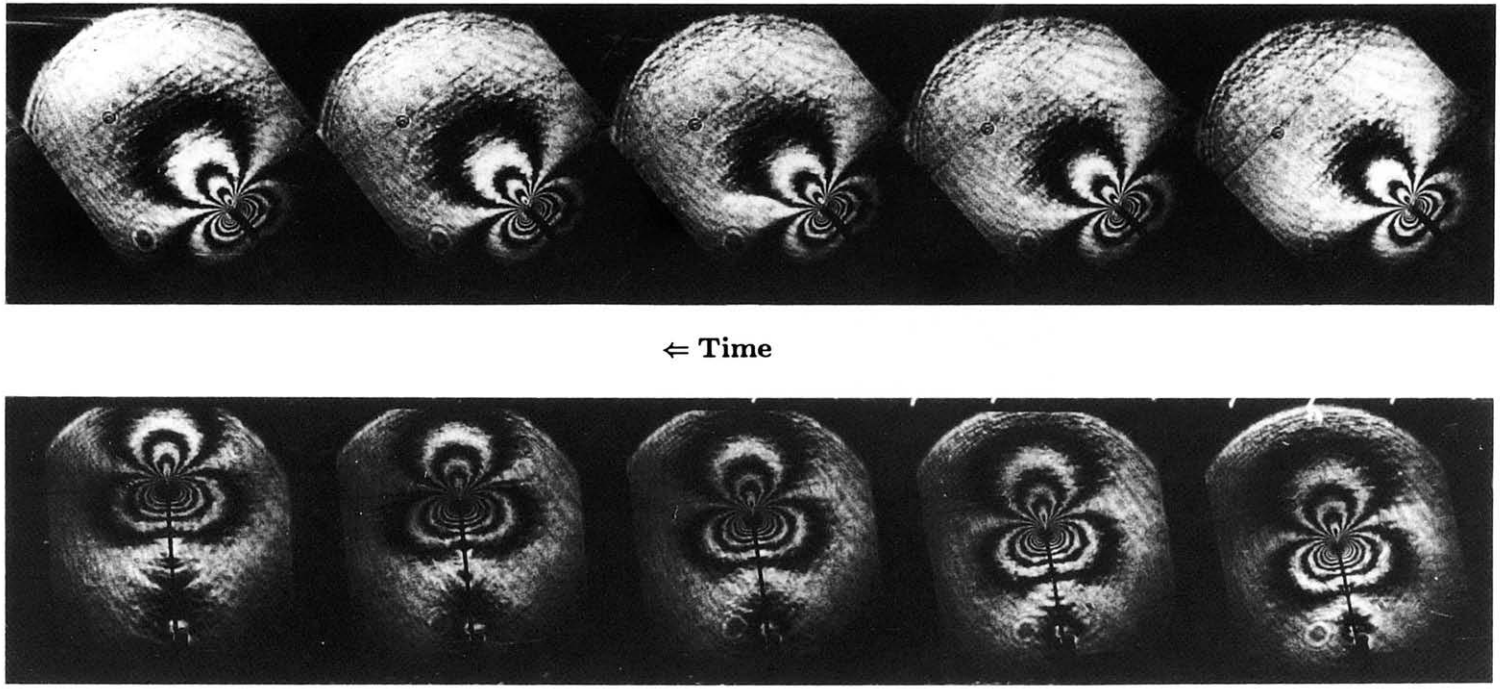

FIG. 14. Sequence of reflection CGS x_1-gradient fringe patterns for a dynamically propagating crack in reflective PMMA specimen (PD-16).

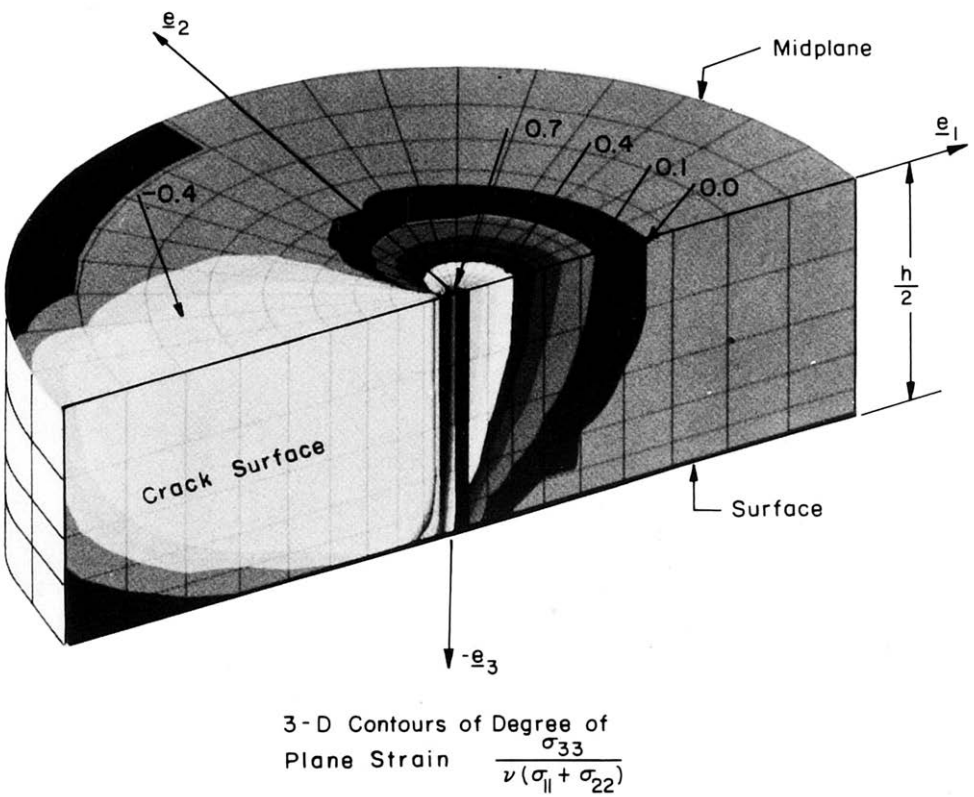

FIG. 16. Three-dimensional contour map showing degree of plane strain in the near-tip region of a three-point bend specimen [from KRISHNASWAMY *et al.* (1988)].

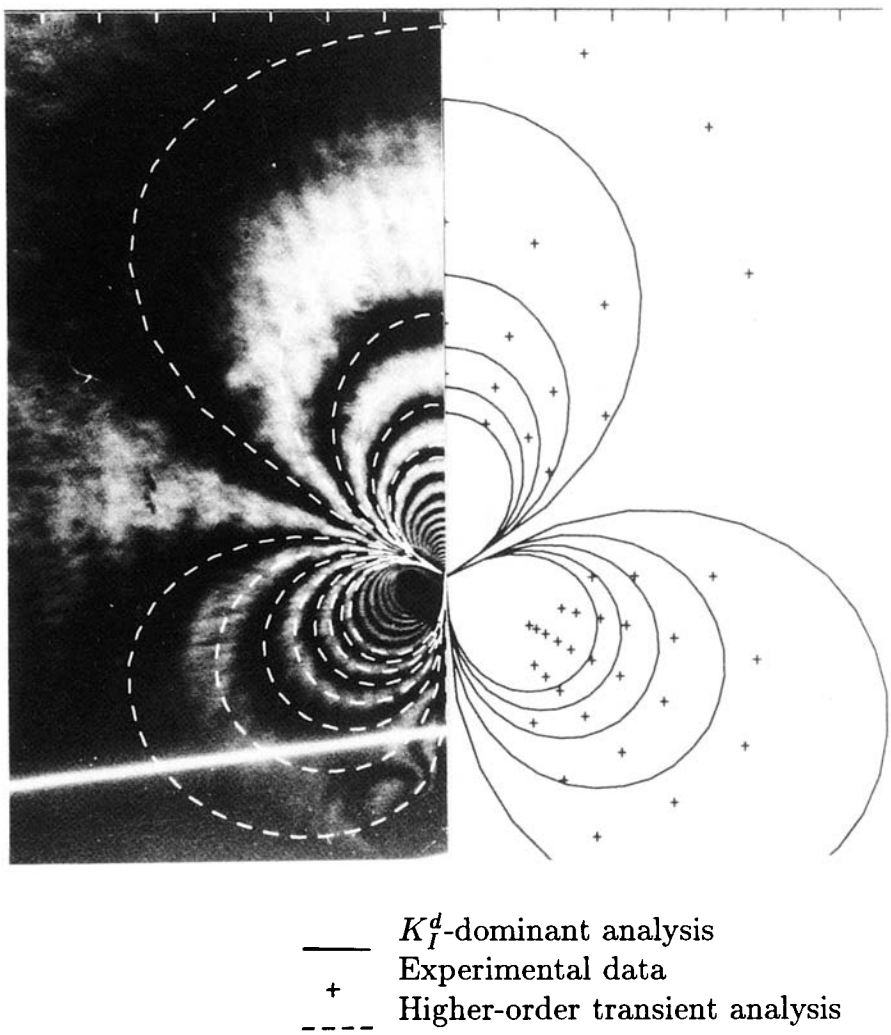

FIG. 18. Synthetic fringe patterns reconstructed from one-term (solid lines) and higher-order (broken lines) transient analysis superposed on the corresponding transmission mode x_1-gradient CGS interferogram for specimen (PD-11).

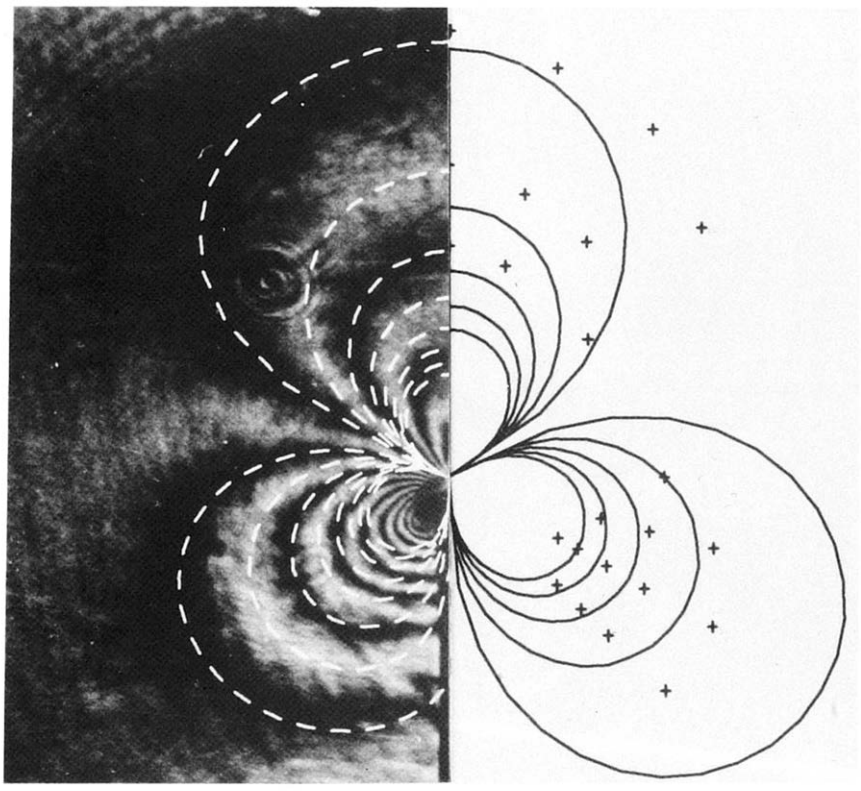

FIG. 21. Synthetic fringe patterns reconstructed from one-term (solid lines) and higher-order (broken lines) transient analysis superposed on the corresponding reflection mode x_1-gradient CGS interferogram for specimen (PD-16).

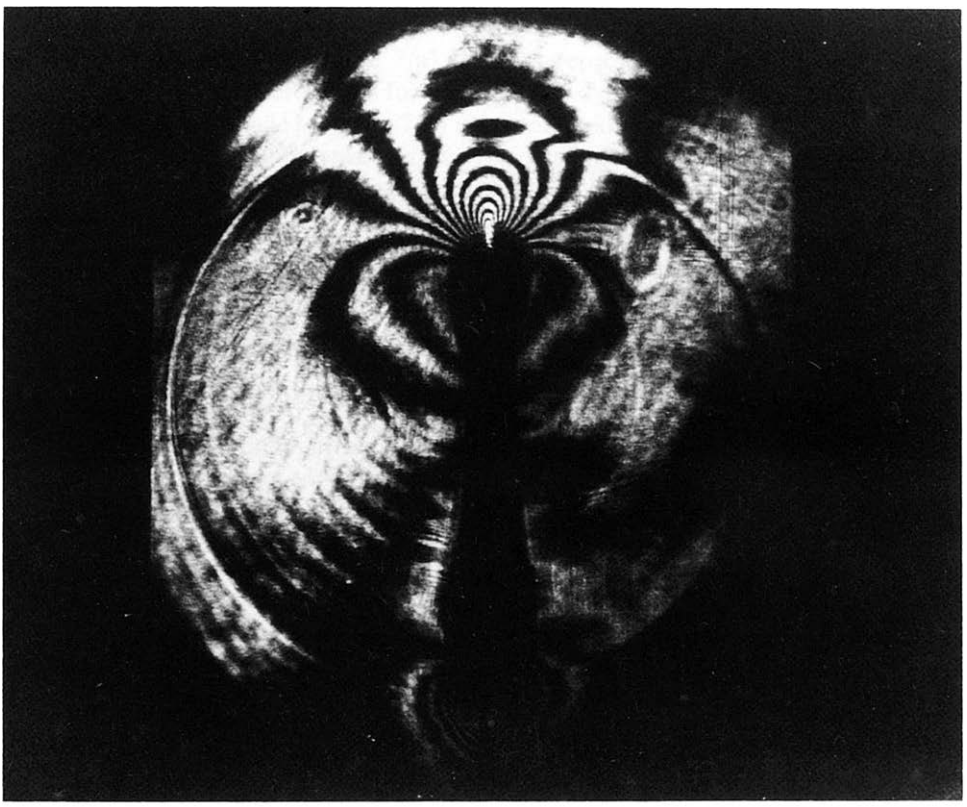

FIG. 23. Reflection mode x_1-gradient CGS fringe pattern for a rapidly propagating crack in AISI 4340 steel specimen (MD-3) showing strong influence of stress waves.

$$\hat{\sigma}_{\alpha\beta}(r,\phi) = \frac{K_I^d(t)}{\sqrt{2\pi r}} \Sigma_{\alpha\beta}^I(\phi,\dot{a}) + O(1), \quad \text{as } r \to 0, \tag{26}$$

where (r,ϕ) is a polar coordinate system travelling with the crack-tip, and $\Sigma_{\alpha\beta}^I$ are known universal functions of ϕ and crack velocity $\dot{a}$ (with respect to some fixed coordinate frame). Indeed, $K_I^d(t)$, the so-called dynamic stress-intensity factor in mode I, is the only factor which is dependent on the specific geometry and loading conditions. Any finite region around the crack tip where the above *asymptotic* field dominates (to within some acceptable error) will be referred to as a K_I^d-dominant region.

4.1.1. *Transmission mode.* Figure 7(a) shows a representative sequence of CGS (transmission mode) interferograms for the case of a dynamically propagating crack in PMMA specimen (PD-11). Figure 7(b) is an enlarged version of one of the interferograms from the above sequence showing the details of the near-tip fringes. Figure 7(c) shows the time history of crack-tip location from which it is seen that the crack propagated with an essentially constant velocity of about 0.25 times the shear wave speed of the material. These fringe patterns correspond to the case when the diffraction gratings were oriented with their principal directions parallel to the x_1-axis. Thus, the fringes surrounding the crack tip at each time represent the x_1-gradient of $(\hat{\sigma}_{11}+\hat{\sigma}_{22})$. In Fig. 8, a sequence of transmission mode CGS interferograms for PMMA specimen (PD-18) is shown. Here, the diffraction gratings were oriented so as to obtain the x_2-gradient of $(\hat{\sigma}_{11}+\hat{\sigma}_{22})$.

The fringe patterns were digitized for analysis to get the fringe order (m or n) and location (r,ϕ) with respect to the crack tip at each instant in time. As previously mentioned, the spatial location (r,ϕ) is inherently uncertain to within $\delta = \Delta \tan\theta$ in the direction of shearing. For typical experimental parameters this amounted to an uncertainty of about 0.6 mm. Note that the *percent* uncertainty in radial location r is lower for the outer fringes than for the fringes closer to the crack tip.

If we now assume that the crack-tip fields are K_I^d-dominant, we find, using (26) in the fringe relations (15) and (16) that

$$ch\mathscr{D}(\dot{a}) \frac{K_I^d}{\sqrt{2\pi}} r_I^{-3/2} \cos(3\phi_I/2) + O(r^{-3/2}) = \frac{mp}{\Delta}, \tag{27}$$

$$ch\mathscr{D}(\dot{a}) \frac{K_I^d}{\sqrt{2\pi}} r_I^{-3/2} \sin(3\phi_I/2) + O(r^{-3/2}) = \frac{np}{\Delta}, \tag{28}$$

where a negative sign has been absorbed into the fringe orders. In the above

$$\mathscr{D}(\dot{a}) = \frac{(1+\alpha_s^2)(\alpha_I^2-\alpha_s^2)}{4\alpha_I\alpha_s-(1+\alpha_s^2)^2}, \tag{29}$$

$$\phi_I = \tan^{-1}(\alpha_I \tan\phi), \tag{30}$$

$$r_I = r\cos\phi(1+\alpha_I\tan^2\phi), \tag{31}$$

$$\alpha_{I,S} = \left[1-\left(\frac{\dot{a}}{c_{I,S}}\right)^2\right]^{1/2}, \tag{32}$$

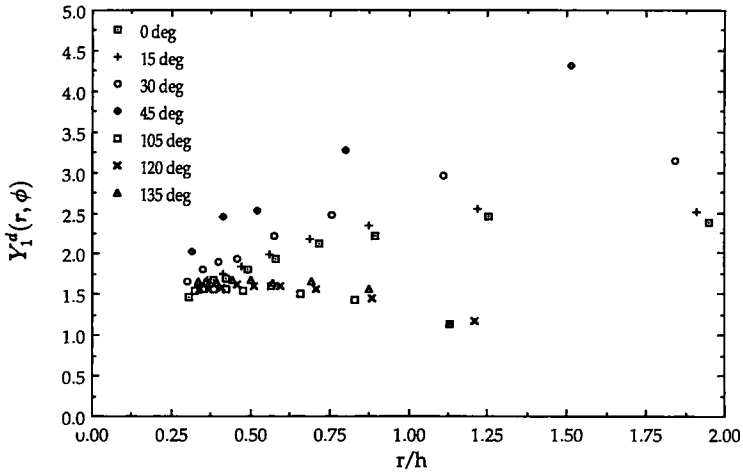

FIG. 9. Radial variation of $Y_1^d(r,\phi)$ along various ϕ for a dynamically propagating crack in PMMA specimen (PD-11) corresponding to 20 μs from crack initiation when crack length to plate width ratio $a/w = 0.23$.

and c_l and c_s are the longitudinal and shear wave speeds, respectively, of the material. Now let us define two functions $Y_1^d(r,\phi)$ and $Y_2^d(r,\phi)$ as follows:

$$Y_1^d(r,\phi) = \left(\frac{mp}{\Delta}\right)\frac{\sqrt{2\pi}}{ch\mathscr{D}(\dot{a})}\frac{r_l^{3/2}}{\cos(3\phi_l/2)}, \tag{33}$$

$$Y_2^d(r,\phi) = \left(\frac{np}{\Delta}\right)\frac{\sqrt{2\pi}}{ch\mathscr{D}(\dot{a})}\frac{r_l^{3/2}}{\sin(3\phi_l/2)}. \tag{34}$$

It is apparent from the above and (27) and (28) that, in regions where K_I^d-dominance holds, Y_α^d would be a constant equal to the instantaneous dynamic stress-intensity factor K_I^d to within experimental error.

Figure 9 shows a typical plot of Y_1^d against normalized radial distance (r/h) for one particular specimen (PD-11) for a time instant a few microseconds after crack initiation. As is apparent from Fig. 9, there appears to be *no* region around the crack tip over which the function Y_1^d is constant. Indeed the spread in Y_1^d values from different locations is as much as 400%. Obviously, extraction of the dynamic stress-intensity factor value cannot be based here on a simplistic assumption of near-tip K_I^d-dominance. One other interesting point must be made. The instantaneous crack length a to plate width w ratio at the time shown in Fig. 9 was $a/w = 0.23$. The immediate question that arises is: would there be a region of *static* K_I-dominance around the crack tip for the case of a *statically* loaded specimen of the same geometry? The answer is provided in Fig. 10 which shows a plot of the static counterparts of the quantities plotted in Fig. 9 for the case of a specimen (PS-9) with $a/w = 0.2$. In the region $(r/h) < 0.5$, Y_1^{static} does not seem to be constant and thus the field in this region does not appear to be K_I-dominant. This is consistent with other experimental

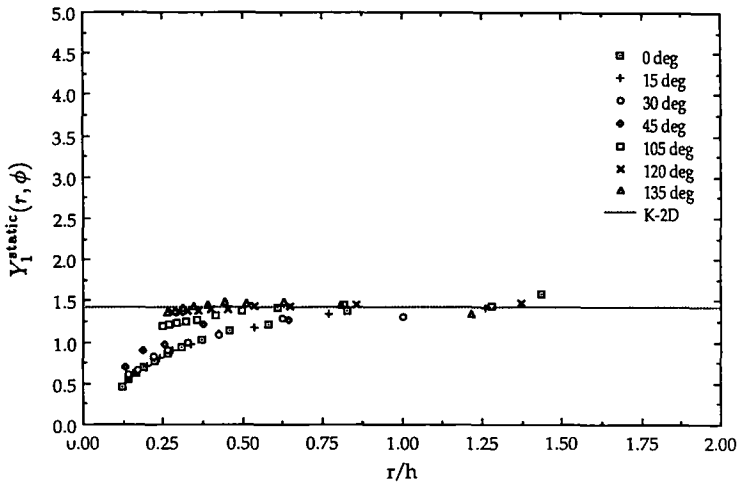

FIG. 10. Radial variation of $Y_1^{static}(r, \phi)$ along various ϕ for a statically loaded crack in PMMA specimen (PS-9) with crack length to plate width ratio $a/w = 0.2$.

investigations wherein such deviation has been attributed to near-tip three-dimensionality (ROSAKIS and RAVI-CHANDAR, 1986; NIGAM and SHUKLA, 1988). Outside this three-dimensional region, however, there appears to be sizeable region of constant Y_1^{static} in the range $0.5 \leqslant (r/h) \leqslant 1.25$. Further, the constant value of Y_1^{static} in this range is in good agreement with the static stress intensity factor K_I^{2D} as obtained from applied boundary load measurements. This is a clear indication that *even though a specimen might exhibit a sizeable region of* K_I*-dominance under static loading conditions, there might be no corresponding region of* K_I^d*-dominance under dynamic conditions.*

In Fig. 11 a plot of Y_2^d against normalized radial distance (r/h) is shown from the x_2-gradient CGS interferogram for specimen (PD-18) for a time instant about 7 μs after crack initiation. The angular spread of Y_2^d values in this case is less than that observed for Y_1^d. The reason for this lies in the different ways in which the higher-order terms affect the x_1- and x_2-gradient fields. It can be shown that the higher-order terms affecting Y_2^d have a weaker angular dependence *in the region of measurement* ($\phi = 30$–$90°$), with Y_2^d being different from K_I^d primarily in magnitude in this region. The corresponding phenomenon for the *static* case is discussed more quantitatively in TIPPUR *et al.* (1988b). To avoid digressing into the details of that discussion, we will cite only the conclusions which are applicable to the dynamic case: *the issue of* K_I^d*-dominance depends on the field quantity under consideration, with higher-order terms affecting different field quantities differently.*

Thus far we have seen that K_I^d-dominance does not appear to hold for a dynamically propagating crack, at least for times immediately after crack initiation. The initiation of a crack from a pre-cut notch is expected to be a *highly transient* event, and this could be one source of the observed lack of K_I^d-dominance in the experiments. If so, could a K_I^d-dominant region develop around the propagating crack tip once the initiation transients have attentuated? From Fig. 12, which is a plot of Y_1^d vs (r/h)

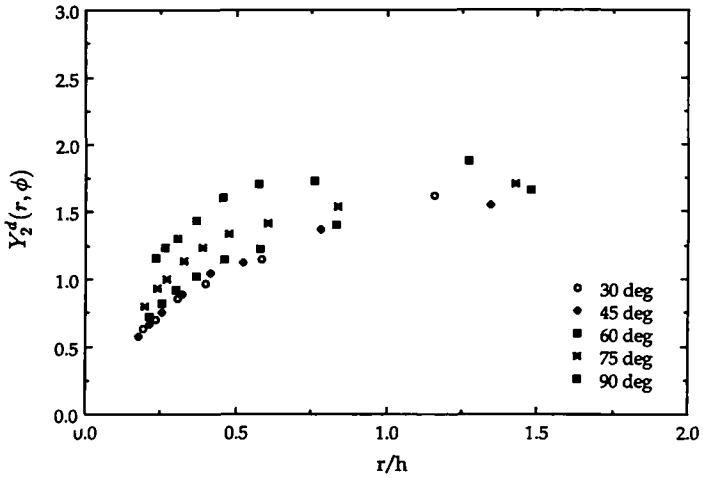

FIG. 11. Radial variation of $Y_2^d(r,\phi)$ along various ϕ for a dynamically propagating crack in PMMA specimen (PD-18).

along $\phi = 0°$ for a specimen (PD-11) for different *times* from crack initiation, it does appear that, as the initiation transients die out, the variation in Y_1^d along $\phi = 0°$ tends to decrease. However, comparison with Y_1^d values along *other* radial lines (Fig. 13) at later times indicates that continuing higher-order transient effects and possible boundary interaction with the crack tip preclude the establishment of a truly K_I^d-dominant region for this specimen/loading configuration.

The observed lack of K_I^d-dominance outside the near-tip three-dimensional region could be due to many reasons. Fundamentally, it could be that the highly transient nature of the deformation field in this finite geometry necessitates a more full-field

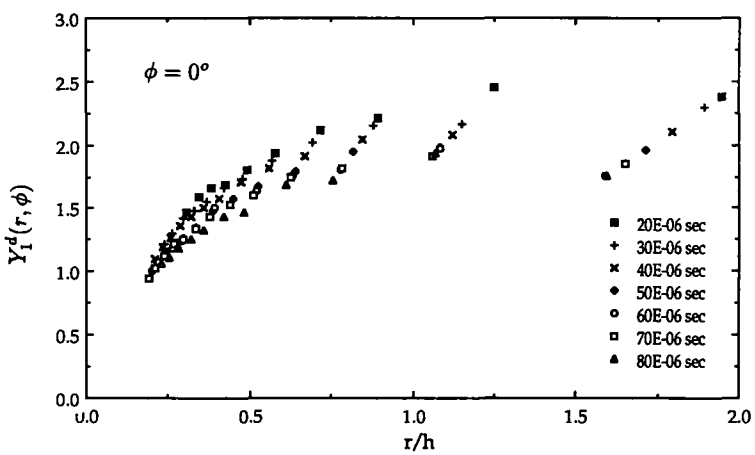

FIG. 12. Radial variation of $Y_1^d(r, \phi)$ along $\phi = 0°$ for various times during dynamic crack propagation in PMMA specimen (PD-11).

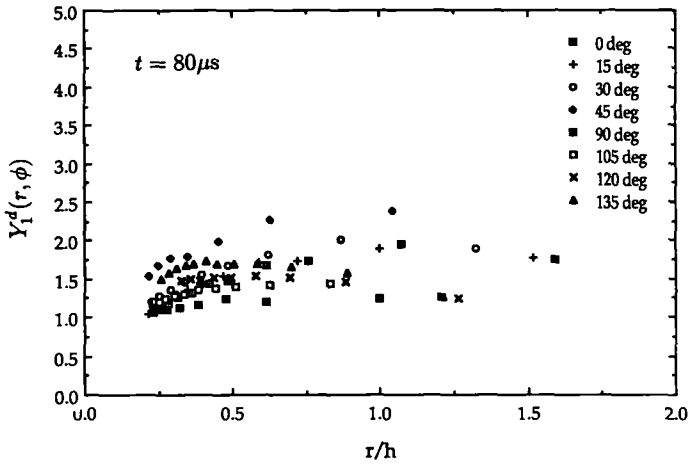

FIG. 13. Radial variation of $Y_1^d(r,\phi)$ along various ϕ for a dynamically propagating crack in PMMA specimen (PD-11).

description of the crack-tip fields. In addition, there is a possibility of rate effects affecting the properties of the material. If the *mechanical* properties of the material are strongly rate-dependent, then one might have to use not an elastic analysis, but a viscoelastic one. For PMMA, however, the viscoelastic response, especially at the high loading rates and short time scales under consideration, is expected to be essentially glassy (FERRY, 1980). If, on the other hand, the rate dependence of the *optical* properties (especially D_1) is strong, then the apparent lack of K_I^d-dominance could be an artifact of the choice of a *transmission* optical technique. In order to rule out this latter possibility, dynamic crack-tip fields in the same material (PMMA) were mapped using CGS in *reflection* mode.

4.1.2. *Reflection mode.* Figure 14 shows a sequence of the x_1-gradient fringe patterns for PMMA specimen (PD-16) in reflection mode. Interpretation of these fringes is once again done assuming K_I^d-dominance, under which the reflection mode fringe relations (24) and (25) become

$$\frac{vh}{2E}\mathscr{D}(\dot{a})\frac{K_I^d}{\sqrt{2\pi}}r_I^{-3/2}\cos(3\phi_I/2)+O(r^{-3/2})=\left(\frac{mp}{2\Delta}\right), \tag{35}$$

$$\frac{vh}{2E}\mathscr{D}(\dot{a})\frac{K_I^d}{\sqrt{2\pi}}r_I^{-3/2}\sin(3\phi_I/2)+O(r^{-3/2})=\left(\frac{np}{2\Delta}\right). \tag{36}$$

Now define the functions

$$Z_1^d(r,\phi)=\left(\frac{mp}{2\Delta}\right)\frac{1}{\mathscr{D}(\dot{a})}\frac{2E\sqrt{2\pi}}{vh}\frac{r_I^{3/2}}{\cos(3\phi_I/2)}, \tag{37}$$

$$Z_2^d(r,\phi)=\left(\frac{np}{2\Delta}\right)\frac{1}{\mathscr{D}(\dot{a})}\frac{2E\sqrt{2\pi}}{vh}\frac{r_I^{3/2}}{\sin(3\phi_I/2)}. \tag{38}$$

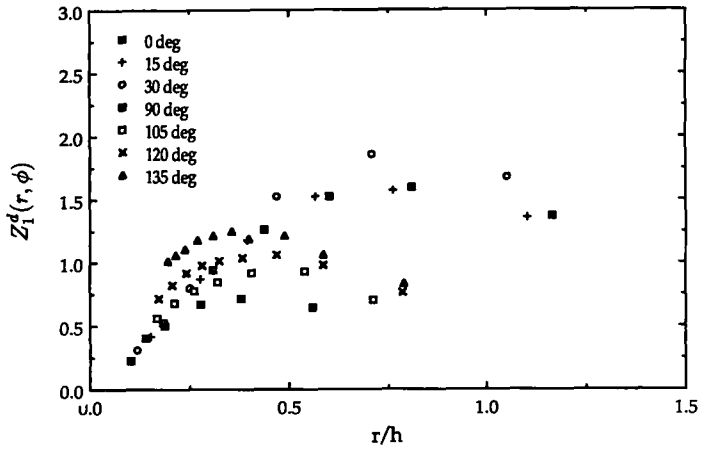

FIG. 15. Radial variation of $Z_1^d(r, \phi)$ along various ϕ for a dynamically propagating crack in reflective PMMA specimen (PD-16).

Once again, in regions of K_I^d-dominance, Z_α^d would be a constant identically equal to the value of instantaneous dynamic stress-intensity factor.

In Fig. 15, the function Z_1^d is plotted against (r/h) for one particular instant during crack propagation in PMMA specimen (PD-16). Once again, we note that there is no region around the crack tip where this function is a constant, indicating that the crack-tip fields were not K_I^d-dominant. Thus it is clear that the observed lack of K_I^d-dominance in the PMMA *transmission* CGS experiments cannot solely be attributed to the rate dependence of the stress-optic coefficient. Indeed, we will see in the next section that the CGS interferograms can be consistently interpreted on the basis of higher-order, *elastodynamic* fields, which would therefore seem to preclude rate effects (on mechanical or optical properties) as being the source of the observed lack of K_I^d-dominance.

4.2. *Fringe interpretation using higher-order description of fields*

While dynamic caustic patterns have conventionally been analyzed under the often unverified assumption of K_I^d-dominance, the use of higher-order terms has been the recent practice in the method of photoelasticity (DALLY *et al.*, 1985). However, all available higher-order elastodynamic solutions thus far have been for the case of steadily propagating cracks, and the applicability of such solutions to possibly highly transient problems has been questioned. Indeed, the main criticism of this approach has been that such a procedure may result in inappropriate time averaging of field quantities (KNAUSS and RAVI-CHANDAR, 1985).

In the following, we will relax the assumptions of near-tip K_I^d-dominance and steady-state crack propagation. We will show that the experimentally obtained transmission and reflection mode CGS interferograms can be successfully interpreted on the basis of a transient, higher-order stress field for a propagating crack that has become available recently (FREUND and ROSAKIS, 1990). In addition, we will also

identify the conditions under which dynamic crack propagation data can possibly be analyzed under a higher-order steady-state approximation.

4.2.1. *Transient higher-order analysis.* FREUND and ROSAKIS (1990) have extended the earlier interior asymptotic solution of FREUND and CLIFTON (1974) to provide a higher-order description of the transient stress state at the vicinity of a dynamically propagating crack. Specializing their results to the case of constant crack velocity appropriate to our experiments [see Fig. 7(c)], we find that the higher-order expression for $(\hat{\sigma}_{11}+\hat{\sigma}_{22})$ needed in the evaluation of fringe relations (15), (16), (24) and (25) is given by

$$\begin{aligned}
\frac{\hat{\sigma}_{11}+\hat{\sigma}_{22}}{2\rho(c_l^2-c_s^2)} &= \frac{3a^2}{4c_l^2}A_0\cos(\phi_l/2)r_l^{-1/2}+\frac{2\dot{a}^2}{c_l^2}A_1 \\
&+\left\{\left[\frac{15\dot{a}^2}{4c_l^2}A_2+\left(1-\frac{\dot{a}^2}{2c_l^2}\right)D^1(A_0)\right]\cos(\phi_l/2)+\frac{\dot{a}^2}{8c_l^2}D^1(A_0)\cos(3\phi_l/2)\right\}r_l^{1/2} \\
&+\left\{\left[\frac{6\dot{a}^2}{c_l^2}A_3+\left(1-\frac{\dot{a}^2}{4c_l^2}\right)D^1(A_1)\right]\cos(\phi_l)\right\}r_l \\
&+\left\{\left[\frac{35\dot{a}^2}{4c_l^2}A_4+\left(1-\frac{\dot{a}^2}{2c_l^2}\right)D^1(A_2)+\frac{1}{9}\left(1-\frac{\dot{a}^2}{4c_l^2}\right)D^2(A_0)+\left(1-\frac{\dot{a}^2}{2c_l^2}\right)\ddot{A}_0\right]\right. \\
&\times\cos(3\phi_l/2)+\left[\frac{3\dot{a}^2}{8c_l^2}D^1(A_2)+\frac{1}{6}\left(1-\frac{\dot{a}^2}{4c_l^2}\right)D^2(A_0)+\frac{3\dot{a}^2}{8c_l^2}\ddot{A}_0\right]\cos(\phi_l/2) \\
&\left.+\left[\frac{\dot{a}^2}{96c_l^2}D^2(A_0)\right]\cos(5\phi_l/2)\right\}r_l^{3/2}+\left\{\left[\frac{12\dot{a}^2}{c_l^2}A_5+\left(1-\frac{\dot{a}^2}{2c_l^2}\right)D^1(A_3)\right.\right. \\
&+\frac{D^2(A_1)}{16}+\left(1-\frac{\dot{a}^2}{2c_l^2}\right)\ddot{A}_1\left.\right]\cos(2\phi_l)+\left[\frac{\dot{a}^2}{2c_l^2}D^1(A_3)+\frac{1}{8}\left(1-\frac{\dot{a}^2}{4c_l^2}\right)D^2(A_1)\right. \\
&\left.\left.+\frac{\dot{a}}{2c_l^2}\ddot{A}_1\right]\right\}r_l^2+O(r_l^2),
\end{aligned} \tag{39}$$

where

$$D^1(A_k)=-\frac{(k+3)\dot{a}}{c_l^2\alpha_l^2}\frac{\mathrm{d}}{\mathrm{d}t}(A_k),\quad k=0,1,2,\ldots,\quad D^2(A_k)=D^1[D^1(A_k)],$$

$$\ddot{A}_k=\frac{1}{c_l^2\alpha_l^2}\left(\frac{\mathrm{d}^2}{\mathrm{d}t^2}A_k\right), \tag{40}$$

and ρ is the density of the material. Although the above expression is for the special case of constant crack velocity, the coefficients A_k in the above transient field are allowed to be time-varying as opposed to the steady-state approximation where the corresponding coefficients must be constant. Note also that the *spatial variation* of the terms associated with coefficients A_k are identical to the ones that would be

obtained from a higher-order *steady-state* analysis with A_0 being related to the dynamic stress-intensity factor and so on. Furthermore, it is seen that the higher-order transient expression contains additional terms whose coefficients depend on time derivatives of lower-order coefficients. For example, $D^1(A_0)$ is proportional to the first time derivative of the stress-intensity factor history and so on.

4.2.1.1. *Transmission mode.* Using the transient field given in (39) in the x_1-gradient transmission mode fringe relation (15), and re-arranging terms, we get an expression of the form

$$\left(\frac{mp}{\Delta}\right)\frac{1}{\mathscr{D}(\dot{a})}\frac{\sqrt{2\pi}}{ch}\frac{r_I^{3/2}}{\cos(3\phi_I/2)} = K_I^d + \left[\beta_2\frac{\cos(\phi_I/2)}{\cos(3\phi_I/2)} + \beta_3\frac{\cos(5\phi_I/2)}{\cos(3\phi_I/2)}\right]r_I + \left[\beta_4\frac{1}{\cos(3\phi_I/2)}\right]r_I^{3/2} + \left[\beta_5\frac{\cos(\phi_I/2)}{\cos(3\phi_I/2)} + \beta_6 + \beta_7\frac{\cos(7\phi_I/2)}{\cos(3\phi_I/2)}\right]r_I^2 + \left[\beta_8\frac{\cos(\phi_I)}{\cos(3\phi_I/2)}\right]r_I^{5/2} + O(r^3), \quad (41)$$

where K_I^d, the dynamic stress-intensity factor, as well as $\beta_2 \ldots \beta_8$ are constants to be determined. The left-hand side of (41) is nothing but the function Y_1^d defined in (33). Under K_I^d-dominance, Y_1^d would have been a constant equal to the instantaneous stress-intensity factor K_I^d. If significant higher-order transient terms exist, then the variation of Y_1^d would be given by the right-hand side of (41), which for simplicity will be denoted by $G_1^d(r, \phi; K_I^d, \beta_2 \ldots, \beta_8)$.

A least-squares procedure analogous to the one described by TIPPUR *et al.* (1989b) was used to fit the above *function* G_1^d to the *experimental data* Y_1^d obtained from the CGS interferograms. Since (39) is obtained from a two-dimensional analysis, data from the near tip three-dimensional region were excluded. This was done using the results from a three-dimensional elastodynamic finite-element analysis of this specimen configuration as described in KRISHNASWAMY *et al.* (1988). The three-dimensional region excluded was based on a cutoff value for the degree of plane strain (which, strictly, should be zero in regions of plane stress) as shown in Fig. 16.

Figure 17 shows the results for one particular time instant during crack propagation in specimen (PD-11). The agreement between the fitted function G_1^d [based on the transient expansion (39) to $O(r^2)$] and the experimental data in Fig. 17 are indeed seen to be remarkably good. Figure 18 conveys a more visual picture of the agreement between the transient analysis and the data. Here, a reconstructed fringe pattern from the fitted function G_1^d is shown superposed (as broken lines) on one side of the corresponding CGS interferogram. Also shown on the other side as solid lines is the reconstructed fringe pattern obtained from a least-squares analysis based on the assumption of K_I^d-dominance [equivalent to using only one term in (39)]. The crosses on this side represent the experimental data obtained from the CGS interferogram. It is seen that the transient analysis agrees very well with the experimental data in the range ($0.5 < r/h < 2.0$, $-\pi < \phi < \pi$), whereas the K_I^d-dominance assumption is clearly inadequate. This was seen to be the case for other time instants as well. This conclusively shows that *the observed lack of* K_I^d*-dominance in the two-dimensional*

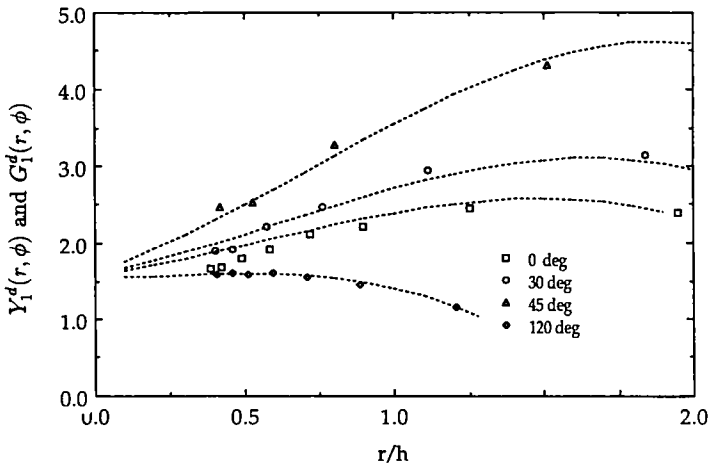

FIG. 17. Comparison of the radial variation of the experimental data $Y_1^d(r, \phi)$ and the analytical fit $G_1^d(r, \phi)$ for various ϕ for transmission mode CGS pattern for specimen (PD-11).

region outside the near-tip three-dimensional zone is due to the important contribution of higher-order terms to the total stress and deformation fields around the crack tip.

The errors associated with interpretation of experimental data on the basis of K_I^d-dominance can now be evaluated. Figure 19 shows the time variation of the dynamic stress-intensity factor during crack propagation in specimen (PD-11) as obtained from the time sequence of x_1-gradient CGS fringe patterns. The solid line represents the value for the dynamic stress-intensity factor when the fringes were interpreted on the basis of the higher-order transient analysis. The dotted line corresponds to the value

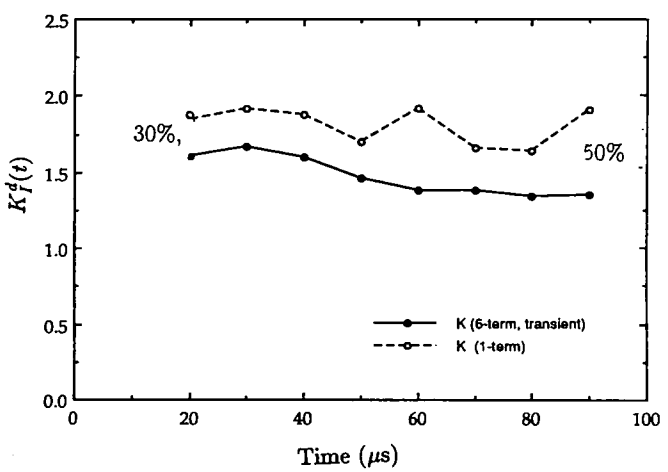

FIG. 19. Time variation of the dynamic stress-intensity factor as obtained from one-term (broken lines) and higher-order (solid lines) transient analysis of CGS sequence for specimen (PD-11).

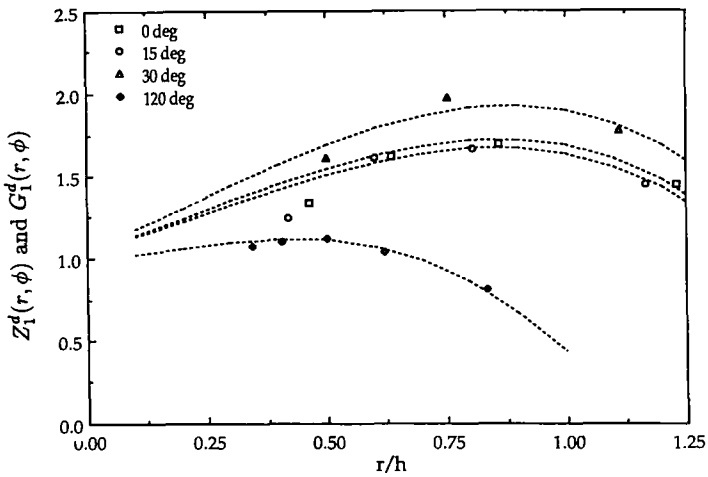

FIG. 20. Comparison of the radial variation of the experimental data $Z_1^d(r, \phi)$ and the analytical fit $G_1^d(r, \phi)$ for various ϕ for reflection mode CGS pattern for specimen (PD-16).

for the dynamic stress-intensity factor obtained when the fringes were analyzed under the assumption of K_I^d-dominance. It is clear that interpretation of experimental data on the basis of K_I^d-dominance leads to substantial errors in the measured values for the dynamic stress-intensity factor.

4.2.1.2. *Reflection mode.* A higher-order analysis of reflection mode CGS interferograms can be done along essentially the same lines as described above. Using the higher-order expression for stresses from (39) in the reflection mode fringe relation (24) leads after rearrangement to

$$\left(\frac{mp}{2\Delta}\right)\frac{1}{\mathscr{D}(\dot{a})}\frac{2E\sqrt{2\pi}}{vh}\frac{r_I^{3/2}}{\cos(3\phi_I/2)} = G_1^d(r, \phi; K_I^d, \beta_2 \ldots \beta_8), \tag{42}$$

where G_1^d is the same expression as the right-hand side of (39) and the left-hand side of (42) is the quantity Z_1^d previously defined in (37). Once again, the experimental data Z_1^d can be fitted to the function G_1^d through the least-squares procedure discussed earlier.

Figure 20 shows the reflection mode CGS results for one particular time instant during crack propagation in a PMMA specimen (PD-16). As in the transmission mode case, the agreement between the fitted function G_1^d and the data Z_1^d is good outside the near-tip three-dimensional region. This is more graphically brought out in Fig. 21 where the reconstructed fringe pattern from the higher-order analysis is shown superposed (as broken lines) on the CGS interferogram on half of Fig. 21. Also shown on the other side of Fig. 21 as solid lines is the reconstructed fringe pattern obtained from a least-squares analysis based on the assumption of K_I^d-dominance. The crosses on this side represent the experimental data obtained from the CGS interferogram. Again, it is seen that K_I^d-dominance assumption is clearly inadequate.

We thus note that *a consistent interpretation of both transmission and reflection mode CGS fringe patterns is possible through inclusion of transient, higher-order effects.*

4.2.2. *Steady-state higher-order analysis.* We next look at the possible applicability of higher-order, steady-state elastodynamic solutions (DALLY *et al.*, 1985) in the interpretation of CGS fringe patterns. A detailed examination of the transient, higher-order stress field [(39)] indicates that the use of a steady-state, higher-order expansion would be appropriate only when: (i) the time derivatives of the coefficients corresponding to the higher-order steady-state terms are all negligibly small, and (ii) the crack velocity is essentially constant. Intuitively, these conditions imply that the crack-tip state is relatively quiescent. If the dynamic crack propagation event is deemed quiescent, we may analyze the CGS interferograms on the basis of the *steady state*, higher-order expansion for the stress field, the results of which should be accepted only if the use of such a procedure can be justified *post facto*.

Using the results of DALLY *et al.* (1985) for the stress field in the fringe relations (15) and (16) we find, on rearrangement of terms, that

$$\left(\frac{mp}{\Delta}\right)\frac{1}{\mathscr{D}(\dot{a})}\frac{\sqrt{2\pi}}{ch}\frac{r_I^{3/2}}{\cos(3\phi_I/2)} = K_I^d + \sum_{N=3}^{\infty} A_N r_I^{(N-1)/2}\frac{\cos\left(\frac{N}{2}-2\right)\phi_I}{\cos(3\phi_I/2)}, \tag{43}$$

$$\left(\frac{np}{\Delta}\right)\frac{1}{\mathscr{D}(\dot{a})}\frac{\sqrt{2\pi}}{ch}\frac{r_I^{3/2}}{\sin(3\phi_I/2)} = K_I^d + \sum_{N=3}^{\infty} A_N r_I^{(N-1)/2}\frac{\sin\left(\frac{N}{2}-2\right)\phi_I}{\sin(3\phi_I/2)}, \tag{44}$$

where the stress-intensity factor K_I^d, and the coefficients of the higher-order terms $A_3 \ldots A_N$ are constants to be determined. Note that the constant term in the expansion for the stress component σ_{11} does not appear above (and hence the lack of the A_2 term). This is because CGS is sensitive to only the *gradients* of stresses. Once again, the left-hand sides of (43) and (44) are the functions Y_α^d, and the right-hand sides will be denoted by $F_\alpha^d(r, \phi, K_I^d, A_3 \ldots A_N)$. As before, the experimental data Y_α^d can be fitted to the function F_α^d by means of a least-squares procedure to extract the various coefficients including the stress-intensity factor. Obviously, the infinite series defining F_α^d needs to be truncated at some point. Unfortunately, since the individual terms of the series are not mutually orthogonal, the values obtained for the corresponding coefficients could be affected by the choice of number of terms used. A consistent scheme for truncation of the series is, therefore, needed. The choice of the optimal number of higher-order terms to use is made here on the basis of a criterion described in detail in TIPPUR *et al.* (1989b). Note that this is not a trivial issue, since it appears that erroneous results could be obtained if substantially more than the optimal number of terms is used.

The sequence of CGS interferograms from specimen (PD-11) were analyzed using the above procedure. Typically a five-term expansion [in (43)] was found to be necessary to adequately describe the crack-tip fields. Figure 22 shows the *time* variation of the dynamic stress-intensity factor and that of the other four higher-order

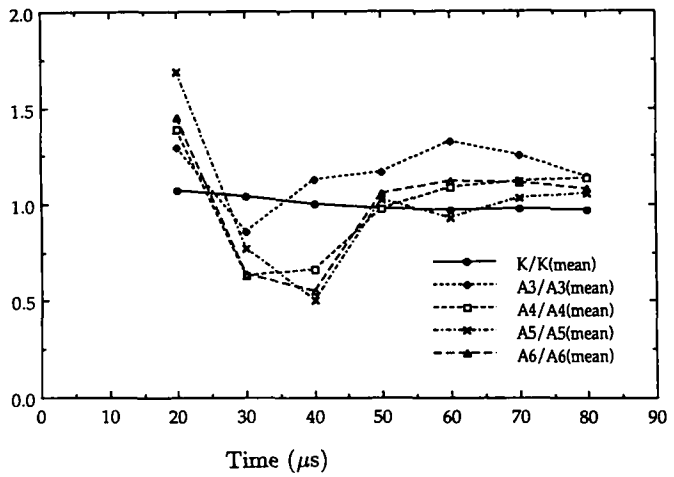

FIG. 22. Time variation of the dynamic stress-intensity factor and coefficient of higher-order terms obtained through a *steady-state* interpretation of CGS sequence for specimen (PD-11). Note that the quantities are normalized by their time-average values for convenience.

coefficients as measured from x_1-gradient CGS interferograms through the least-squares procedure described earlier. For convenience of presentation, the time-varying coefficients have all been normalized by their time-average values. Note that, for times sufficiently close to the crack initiation event, the field does not appear to be very quiescent as indicated by the large variation in the measured coefficients. The use of a steady-state analysis and the consequent results are mutually inconsistent at these early times, and thus the results of the steady-state approximation are not acceptable. However, at later times, the extracted coefficients do not appear to be very strongly time-varying. Also, during the time shown, the crack propagated with essentially a constant velocity of $\dot{a}/c_l \approx 0.13$ [see Fig. 7(c)]. Thus, the use of the higher-order *steady-state* expansion and the consequent results are at least mutually consistent and may not be entirely unjustified at these later times. Of course, for propagation times close to initiation, or whenever the field does not appear to be very quiescent, use of the transient higher-order expansion (39) would be more appropriate.

5. DISCUSSION

The results of this investigation point out the pitfalls associated with the extraction of dynamic fracture data under the assumption of K_I^d-dominance. That violation of assumed K_I^d-dominance could be the source of certain incompatible experimental results in the literature (KALTHOFF, 1983; RAVI-CHANDAR and KNAUSS, 1984; ROSAKIS *et al.*, 1984; NIGAM and SHUKLA, 1988a; ZEHNDER and ROSAKIS, 1989) has been the contention of many recent investigators (DALLY *et al.*, 1985; RAVI-CHANDAR and KNAUSS, 1987; KRISHNASWAMY and ROSAKIS, 1988; KRISHNASWAMY *et al.*, 1988). In particular, it should be noted that this study substantiates the experimental results of

KRISHNASWAMY and ROSAKIS (1988) which dealt with the issue of the effect of lack of K_I^d-dominance on the interpretation of dynamic caustics.

In this paper, we have shown that it is possible to meaningfully interpret dynamic CGS fringe data even in situations of no K_I^d-dominance. To do this, the data outside of the near-tip three-dimensional region must be appropriately interpreted taking into account the contribution of transient, higher-order terms to the total stress and deformation fields around the crack tip. However, there are situations where even this approach fails. This is clearly brought out from the reflection mode CGS interferograms (Fig. 23) for a very rapidly propagating crack in a AISI 4340 steel specimen (MD-3). In particular, note the presence of strong unloading waves as the crack propagates, which are manifested as sharp kinks in the fringes. Of course, assuming K_I^d-dominance in such stress wave dominated situations is not meaningful. It is also inappropriate to use a steady-state higher-order expansion in this case. In fact, even the higher-order transient field [(39)] will not be applicable since it is from a *two-dimensional* analysis and hence does not model possible wave effects on the specimen surface. Interpretation of these fringe patterns will have to take into account the *three-dimensional* transient effects, and can be done possibly only through detailed numerical analyses.

Contrary to conventional wisdom, K_I^d-dominance in the vicinity of a dynamically propagating crack appears to be the exception rather than the rule. It is thus critically important that *interpretation of experimental data under assumed* K_I^d*-dominance, steady-state or two-dimensional conditions be carefully justified prior to attributing physical credence to the observed phenomena.*

6. CONCLUSION

The salient points discussed in this paper can be summarized as follows:

(1) A shearing interferometric technique (CGS) is proposed as a viable alternative to current methods in the experimental study of dynamic crack propagation. CGS is a full-field technique that can be used in reflection mode for opaque materials, and can also be used in transmission mode for optically *isotropic* transparent materials.

(2) Results from dynamic crack propagation in PMMA and AISI 4340 steel specimens show that interpretation of experimental data on the basis of near-tip K_I^d-dominance could lead to substantial errors due both to near-tip three-dimensionality as well as higher-order effects in the two-dimensional region.

(3) It is further shown that a consistent interpretation of experimental data obtained from the two-dimensional region is possible using higher-order analytical description of the transient crack-tip fields.

ACKNOWLEDGEMENTS

The authors would like to thank Professor L. B. Freund of Brown University for his help and encouragement during the course of this investigation. The support of ONR through contracts N0014-85-K-0596 and N00014-90-J-1340 is also acknowledged.

REFERENCES

BALAS, J. and DRZIK, M. 1983 *Stav. Čas.* **31,** 447.

BEINERT, J. and KALTHOFF, J. F. 1981 In *Mechanics of Fracture* (edited by G. SIH), Vol. 7, p. 281. Martinus Nijhoff, The Hague.

DALLY, J. W., FOURNEY, W. L. and IRWIN, G. R. 1985 *Int. J. Fracture* **27,** 159.

FERRY, J. D. 1980 *Viscoelastic Properties of Polymers*, p. 339. John Wiley, New York.

FREUND, L. B. and CLIFTON, R. J. 1974 *J. Elasticity* **4,** 293.

FREUND, L. B. and ROSAKIS, A. J. 1990 Presented at the Eleventh National Congress of Applied Mechanics, Tucson, AZ.

KALTHOFF, J. F. 1983 In *Workshop on Dynamic Fracture* (edited by W. G. KNAUSS, A. J. ROSAKIS and K. RAVI-CHANDAR). Pasadena, CA.

KALTHOFF, J. F. 1985 *Int. J. Fracture* **27,** 277.

KNAUSS, W. G. and RAVI-CHANDAR, K. 1985 *Int. J. Fracture* **27,** 127.

KOBAYASHI, T. and DALLY, J. W. 1977 In *Fast Fracture and Crack Arrest* (edited by G. T. HAHN and M. F. KANNINEN), ASTM STP 627, p. 257.

KRISHNASWAMY, S. and ROSAKIS, A. J. 1988 GALCIT SM-Report 88-21, California Institute of Technology, Pasadena, CA (*J. appl. Mech.* **58,** 87).

KRISHNASWAMY, S., ROSAKIS, A. J. and RAVICHANDRAN, G. 1988 GALCIT SM-Report 88-22, California Institute of Technology, Pasadena, CA (*J. appl. Mech.* **58,** 95).

NIGAM, H. and SHUKLA, A. 1988 *Expl. Mech.* **28,** 123.

RAVI-CHANDAR, K. and KNAUSS, W. G. 1984 *Int. J. Fracture* **25,** 247.

RAVI-CHANDAR, K. and KNAUSS, W. G. 1987 *J. appl. Mech.* **54,** 72.

ROSAKIS, A. J., DUFFY, J. and FREUND, L. B. 1984 *J. Mech. Phys. Solids* **32,** 443.

ROSAKIS, A. J. and RAVI-CHANDAR, K. 1986 *Int. J. Solids Struct.* **22,** 121.

TIPPUR, H. V., KRISHNASWAMY, S. and ROSAKIS, A. J. 1989a GALCIT SM-Report 89-1, California Institute of Technology, Pasadena, CA (*Int. J. Fracture* **48,** 193).

TIPPUR, H. V., KRISHNASWAMY, S. and ROSAKIS, A. J. 1989b GALCIT SM-Report 89-11, California Institute of Technology, Pasadena, CA (to appear in *Int. J. Fracture*).

ZEHNDER, A. T. and ROSAKIS, A. J. 1989 GALCIT SM-Report 88-4, California Institute of Technology, Pasadena, CA (*Int. J. Fracture* **43,** 271).